J. Appl. Comput. Mech., xx(x) (2026) 1-17
DOI: 10.22055/jacm.2026.48717.5450

ISSN: 2383-4536
jacm.scu.ac.ir

Shahid Chamran University of Ahvaz

Journal of Applied and Computational Mechanics



Research Paper

A Linear-shear-stress-based Theoretical Model for Prediction of Adhesive Shear Stress and Dynamic Axial Response in Tubular Adhesive Joints

Ramzi Othman[1], Khalid H. Almitani[2], Shaalan A. Alqarni[2], Georges Challita[3]

[1] Ecole Centrale de Nantes, Institut de Recherche en Génie Civil et Mécanique, UMR CNRS 6183, BP 92101, 44321 Nantes cedex 3, France
[2] Mechanical Engineering Department, Faculty of Engineering, King Abdulaziz University, P.O. Box 80248, Jeddah 21589, Saudi Arabia
[3] Equipe MMC, CRSI, Lebanese University, Faculty of Engineering, Roumieh, El-Metn, Lebanon

Received August 26 2025; Revised June 16 2026; Accepted for publication October 11 2026.
✉ Corresponding author: R. Othman (ramzi.othman@ec-nantes.fr)
© 2026 Published by Shahid Chamran University of Ahvaz

Abstract. The use of adhesives for joining tubular structures has gained significant attention as a replacement for traditional methods such as welding, brazing, and soldering. Adhesive bonding offers several advantages, including reduced manufacturing costs, extended component life, and lower structural weight. This study aims to investigate the mechanical response of adhesively bonded tubular joints under axial loading. A theoretical model is developed based on the assumption that the adherends shear stresses vary linearly with the radial coordinate. The model is employed to predict both the shear stress distribution within the adhesive layer and the natural frequencies associated with axial vibrations. To validate the theoretical predictions, a finite element axisymmetric model is also developed. A good agreement is observed between the theoretical predictions and the numerical results, confirming the reliability of the proposed approach. Moreover, the theoretical model performs best when the ratio of axial stiffness of the adherends to the shear stiffness of the adhesive is high.

Keywords: Tubular joint, Vibration, Harmonic response, Shear-lag, Adhesives, Anchors.

1. Introduction

The use of adhesives in structural joining has been steadily increasing, driven by the need to replace traditional methods such as brazing, welding, and soldering [1]. Compared to these conventional techniques, adhesive bonding offers several advantages, including reduced weight, lower stress concentrations, and cost-effectiveness. Circular axisymmetric structures, which are commonly employed in engineering applications, are often subjected to vibration-related issues [2–4].

Tubular joints are frequently used in sectors such as aviation, marine, and civil construction [5, 6]. They are also prevalent in bonded anchors, where steel or composite anchor rods are secured to concrete using thermosetting structural adhesives [7–9]. Despite the numerous benefits of adhesive bonding, its application is still approached with caution due to the limited availability of reliable data—particularly concerning the vibrational behavior of bonded joints.

Theoretical approaches for predicting the performance of tubular joints are of significant interest, as they can yield closed-form solutions that are particularly valuable in the preliminary stages of design [10]. However, tubular joints have received less attention in the existing literature compared to lap joints [5, 6]. Lubkin and Reissner [11] developed a theoretical model incorporating peel and shear stresses, based on the classical approach introduced by Goland and Reissner [12] for lap joints. Their model accounted for tension, shear, and bending loads applied to the adherend tubes. Later, Shi and Cheng [13] considered axial, radial, hoop, and shear stresses by solving the axial and radial equilibrium equations, assuming a linear variation of axial stresses with respect to the radial coordinate in the adherends.

Nemes et al. [14] and Nemes and Lachaud [15] extended the analysis by developing variational models in which the stress components in the cylindrical assembly were expressed as functions of the axial stress in the first tube. The axial, shear, and hoop stresses in the adherends, as well as shear and hoop stresses in the adhesive, were derived by Nemes et al. [14] from this axial stress, which was assumed to depend only on the axial coordinate. The model was refined by Nemes and Lachaud [15] by additionally accounting for a constant radial stress in the adhesive, while the axial stress in the adhesive was neglected. Their formulation employed cylindrical coordinates to satisfy axial and radial equilibrium conditions. This analytical framework was later adopted by Kumar [16] and Kumar and Scanlan [17] in their investigation of functionally graded tubular adhesive joints, and by Martinez et al. [18] in the analysis of shear stresses in pin-and-collar joints.

Published online: November 05 2026

Additionally, Selahi [19] modeled the adherends as composite laminate shells and represented the adhesive layer using tension/compression and shear springs. Similarly, Kurennov and Dvoretska [20] treated the adherends as shell structures and assumed a linear variation of tangential stress across the adhesive thickness. To describe normal stresses within the adhesive, they employed the two-parameter Vlasov–Pasternak model, treating the adhesive layer as an elastic foundation. Kumar and Khan [21] adopted a different approach by using generic stress functions in combination with the principle of minimum complementary energy to derive the stress distribution in both the adherends and the adhesive layer. Shishesaz et al. [22] modelled the effects of defects on the distribution of adhesive stresses in composite tubular joints.

The incorporation of multiple stress components in theoretical analyses often results in highly complex formulations, which may not yield closed-form solutions. To address this, some researchers have adopted simplified models. Pugno and Carpinteri [23], for example, based their analysis on Volkersen's shear lag model, considering only axial stresses in the adherends and shear stresses in the adhesive. Nayeb-Hashemi et al. [24] also built upon Volkersen's model. However, acknowledging the difference between the inner and outer radii of the adhesive layer, they allowed for a radial variation of shear stress within the adhesive, thereby refining the original assumptions to better reflect the actual stress distribution.

Numerous theoretical studies have focused on modeling the mechanical behavior of tubular adhesive joints under static loading conditions [5, 6, 11–24]. These analytical solutions are highly valuable in the design phase, offering insight into stress distributions. For instance, Spaggiari and Dragoni [25] utilized analytical modeling to optimize functionally graded tubular adhesive joints and reduce stress concentrations within the adhesive layer. In contrast, relatively few studies have addressed the vibration or harmonic response of tubular joints [26–28]. Rao and Zhou [26] applied an energy method combined with Hamilton's principle to analyze the transverse vibration behavior of tubular adhesive joints. Vaziri and Nayeb-Hashemi developed theoretical models for voided tubular joints under dynamic torsional [27] and axial [28] loading. Their investigations highlighted the influence of void size on the natural frequencies of the joint, employing a shear-lag model to account for axial load transfer.

In all of these studies [26–28], theoretical approaches were adopted to capture the vibrational response of tubular joints. Additionally, Gunes et al. [29] conducted a finite element analysis to investigate the three-dimensional vibration behavior of tubular joints composed of functionally graded materials, further contributing to the understanding of their dynamic characteristics.

This study presents a theoretical model for analyzing the axial harmonic response of tubular adhesive joints. The model is developed under the assumption of a linear shear stress distribution through the thickness of the adherends, initially proposed and validated by Tsai et al. [30] for modeling the static response of single-lap and double-lap joints. This assumption has since been adopted in dynamic analyses by Challita and Othman [31] and Gafar et al. [32] to study the harmonic response of lap joints. Challita [33] extended the approach to voided double-lap joints, while Almitani and Othman [34] incorporated adhesive viscoelasticity into the model. The same linear shear stress assumption was also successfully applied to the impact response of composite semi-infinite single-lap joints [35]. More recently, Wang et al. [36] extended the method to include peel stresses in the study of vibrating double-lap joints. Additionally, Sindi et al. [37] extended the method to consider functionally-graded adhesive layer and solved the differential equations using Heun function.

In the present work, this linear adhesive shear stress assumption is employed to derive the governing equations for the axial harmonic response of tubular adhesive joints. The theoretical predictions are validated through comparison with finite element (FE) results obtained using ANSYS.

2. Linear-shear-stress-based Theoretical Model

Theoretical modeling plays a crucial role in deriving closed-form solutions, which are particularly valuable during the preliminary design phase and for gaining insight into the key parameters that govern the mechanical behavior of adhesive joints. In this section, a theoretical model is developed based on the assumption that the shear stress in the adherends varies linearly with the radial coordinate. This assumption offers analytical convenience while capturing the essential features of the stress distribution in tubular adhesive joints.

The present theoretical model represents a compromise between simplicity and accuracy. By employing a one-dimensional kinematic assumption, only the axial displacement is considered, which simplifies the derivation of the governing equations. Unlike classical Volkersen-type models, the proposed formulation accounts for the variation of shear stress in the adherend, improving the accuracy of stress predictions. Two-dimensional models provide more detailed kinematics and account for radial displacement, but result in substantially more complex equations. Therefore, the present approach captures the essential stress distribution in tubular joints while maintaining analytical tractability.



Fig. 1. Overlap region of a tubular joint.



Fig. 2. Axi-symmetric model.

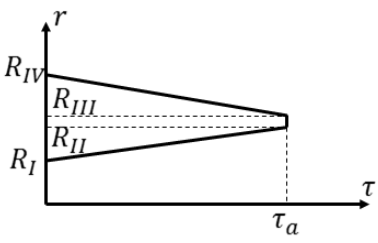


Fig. 3. Shear stress distribution through the joint.

2.1. Governing equations

This study focuses on modeling the mechanical response of tubular adhesive joints. For the sake of simplicity, the analysis begins with the overlap region (Fig. 1), while the two end sections of the tubular structure are incorporated later through appropriate boundary conditions. Taking advantage of the problem's axisymmetric nature [36], the formulation is expressed in terms of radial (r) and axial (x) coordinates, as illustrated in Fig. 2.

The shear stresses within the inner and outer adherends are assumed to vary linearly with the radial coordinate, as depicted in Fig. 3. The assumption of a linear variation of shear stress within the adherends is primarily motivated by boundary condition considerations specific to tubular geometries. In the present configuration, each adherend is subjected to asymmetric boundary conditions across its thickness. For the outer adherend, the external surface is traction-free, while the internal surface must ensure shear stress continuity with the adhesive layer. Conversely, for the inner adherend, the internal surface is traction-free, whereas the external surface must satisfy continuity with the adhesive.

Classical Volkersen-type models, which assume uniform shear stress across the adherend thickness, are therefore unable to simultaneously satisfy these boundary conditions. Introducing a linear variation of shear stress through the radial coordinate allows these essential conditions to be met while preserving analytical tractability. This assumption represents a compromise between physical realism and mathematical simplicity, enabling closed-form solutions without resorting to fully three-dimensional elasticity formulations.

It is acknowledged that for thick-walled tubular adherends or for large diameter-to-thickness ratios, the linear approximation may lose accuracy, as the actual stress distribution may become nonlinear. In such cases, a more refined description could be obtained by subdividing each adherend into multiple thinner coaxial cylindrical layers, within which the shear stress may still be reasonably approximated as linear. This multilayer approach would improve accuracy but would significantly increase model complexity and is therefore considered beyond the scope of the present work. Its development is left for future studies.

Accordingly, the shear stress distributions are defined as:

$$\tau_i(x,r,t)=\tau_a(x,t)\frac{r\text{-}R_I}{t_i}, \tag{1}$$

and,

$$\tau_o(x,r,t)=\tau_a(x,t)\frac{R_{IV}\text{-}r}{t_o}. \tag{2}$$

where t_i and t_o are the thicknesses of the inner and outer adherends, respectively; R_I is the inner radius of the inner adherend, R_{IV} is the outer radius of the outer adherend; and τ_a denotes the adhesive shear stress.

Equations (1) and (2) satisfy the boundary conditions by ensuring that the shear stress vanishes at the inner free surface of the inner adherend and the outer free surface of the outer adherend. Additionally, they guarantee continuity of shear stress at the adhesive interfaces, such that the shear stress at the outer surface of the inner adherend and the inner surface of the outer adherend is equal to $\tau_a(x,t)$, the shear stress in the adhesive layer. This implies a constant shear stress through the adhesive thickness. While this simplification does not capture the exact stress variation, it is considered acceptable due to the thin nature of the adhesive layer. Furthermore, the assumed linear variation ensures that the adhesive shear stress remains continuous across the radial coordinate r, as illustrated in Fig. 3.

Assuming linear elastic behavior for the adherends, the corresponding expressions for the shear strain in the inner and outer tubes can be written as:

$$\gamma_i(x,r,t)=\tau_a(x,t)\frac{r\text{-}R_I}{G_i t_i}, \tag{3}$$

and,

$$\gamma_o(x,r,t)=\tau_a(x,t)\frac{R_{IV}\text{-}r}{G_o t_o}. \tag{4}$$

where G_i and G_o are the shear moduli of the inner and outer adherends, respectively. These expressions allow for the use of different materials for each adherend. In the case of orthotropic composite adherends, G_i and G_o correspond to the shear moduli in the xr-plane (i.e., $G_{xr,i}$ and $G_{xr,o}$). For sake of simplicity, the subscript $_{xr}$ is omitted in the subsequent derivations. Assuming small strains, the adherends' shear strains can be approximated:

$$\gamma_i=\frac{\partial u_i}{\partial r}$$

and,

$$\gamma_o=\frac{\partial u_o}{\partial r}.$$

Consequently, the axial displacements of the inner and outer adherends can be obtained by integrating the shear strain expressions from Eqs. (3) and (4). The resulting expressions are:

$$u_i(x,r,t)=u_{ia}(x,t)+\int_{R_{II}}^{r}\tau_a(x,t)\frac{s\text{-}R_I}{G_i t_i}\,ds, \tag{5}$$

and,

$$u_o(x,r,t)=u_{oa}(x,t)+\int_{R_{III}}^{r}\tau_a(x,t)\frac{R_{IV}\text{-}s}{G_o t_o}\,ds. \tag{6}$$

where u_{ia} and u_{oa} and represent the axial displacements at the adhesive–inner adherend and adhesive–outer adherend interfaces, respectively. Here, R_{II} is the outer radius of the inner adherend, and R_{III} is the inner radius of the outer adherend.

Evaluating the integrals in Eqs. (5) and (6) leads to the following expressions for the axial displacements in the inner and outer adherends:

$$u_i(x,r,t)=u_{ia}(x)+\frac{(r-R_I)^2-t_i^2}{2G_i t_i}\tau_a(x,t), \tag{7}$$

and,

$$u_o(x,r,t)=u_{oa}(x)-\frac{(r-R_{IV})^2-t_o^2}{2G_o t_o}\tau_a(x,t). \tag{8}$$

Applying the small strain approximation, where $\varepsilon_i=\partial u_i/\partial x$ and $\varepsilon_o=\partial u_o/\partial x$, the axial strains in the inner and outer adherends are obtained as:

$$\varepsilon_i(x,r,t)=\frac{\partial u_{ia}}{\partial x}+\frac{(r-R_I)^2-t_i^2}{2G_i t_i}\frac{\partial \tau_a}{\partial x}, \tag{9}$$

and,

$$\varepsilon_o(x,r,t)=\frac{\partial u_{oa}}{\partial x}-\frac{(r-R_{IV})^2-t_o^2}{2G_o t_o}\frac{\partial \tau_a}{\partial x}. \tag{10}$$

Assuming linear elastic behavior for the adherends, the corresponding normal (axial) stresses are given by Hooke's law as:

$$\sigma_i(x,r,t)=E_i\frac{\partial u_{ia}}{\partial x}+E_i\frac{(r-R_I)^2-t_i^2}{2G_i t_i}\frac{\partial \tau_a}{\partial x}, \tag{11}$$

and,

$$\sigma_o(x,r,t)=E_o\frac{\partial u_{oa}}{\partial x}-E_o\frac{(r-R_{IV})^2-t_o^2}{2G_o t_o}\frac{\partial \tau_a}{\partial x}. \tag{12}$$

where E_i and E_o are the Young's moduli of the inner and outer adherends, respectively. In the case of orthotropic composite adherends, the elastic moduli E_i and E_o correspond to $E_{xx,i}$ and $E_{xx,o}$, respectively. For simplicity, the subscript $_{xx}$ will be omitted henceforth. Additionally, E_i and E_o may not necessarily be equal, as the theoretical model accommodates different materials for the two adherends.

The normal/axial force applied on one cross-section of the inner tube is calculated by integrating the normal stress over the entire cross-section:

$$N_i(x,t)=2\pi\int_{R_I}^{R_{II}}\sigma_i(x,r,t)\ r dr. \tag{13}$$

Evaluating this integral yields:

$$N_i(x,t)=E_i\left(S_i\frac{\partial u_{ia}}{\partial x}+\frac{2\pi r_i^3-S_i t_i}{2G_i}\frac{\partial \tau_a}{\partial x}\right). \tag{14}$$

where $r_i=\sqrt[3]{(R_I^3+R_I^2R_{II}-5R_IR_{II}^2+3R_{II}^3)/12}$ is a characteristic radius of the inner adherend and, S_i is the cross-sectional area of the inner tube.

Likewise, the normal/axial force applied on one cross-section of the outer tube is determined by integrating the normal stress over the entire cross-section:

$$N_o(x,t)=2\pi\int_{R_{III}}^{R_{IV}}\sigma_o(x,r,t)\ r dr. \tag{15}$$

Evaluating this integral yields:

$$N_o(x,t)=E_o\left(S_o\frac{\partial u_{oa}}{\partial x}-\frac{2\pi r_o^3-S_o t_o}{2G_o}\frac{\partial \tau_a}{\partial x}\right). \tag{16}$$

where $r_o=\sqrt[3]{(R_{IV}^3+R_{IV}^2R_{III}-5R_{IV}R_{III}^2+3R_{III}^3)/12}$ is a characteristic radius of the outer adherend and, S_o is the cross-sectional area of the outer tube.

Now, consider a differential segment of the tubular overlap region with length dx. By examining the free-body diagram (see Fig. 4) and applying Newton's second law to the inner and outer adherends, the following governing equations are obtained:

$$\frac{\partial N_i}{\partial x}+2\pi R_a\tau_a=2\pi\int_{R_I}^{R_{II}}\rho_i\frac{\partial^2 u_i}{\partial t^2}r dr, \tag{17}$$

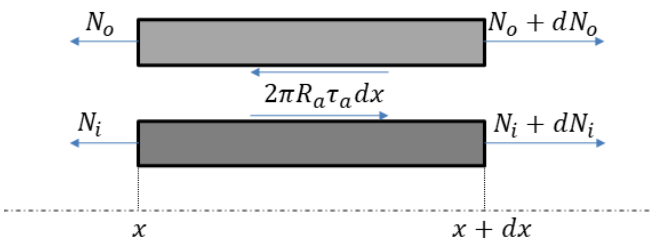


Fig. 4. Free-body diagram of a dx-long tubular joint.

and,

$$\frac{\partial N_o}{\partial x}-2\pi R_a\tau_a=2\pi\int_{R_I}^{R_{II}}\rho_o\ \frac{\partial^2 u_o}{\partial t^2}rdr, \tag{18}$$

where $R_a=\frac{R_{II}+R_{III}}{2}$ is the mid-thickness radius of the adhesive layer, and ρ_i and ρ_o are the mass densities of the inner and outer adherends, respectively.

Given the adhesive layer's small thickness, the shear stress is assumed constant in the radial direction. Under linear elastic behavior, the adhesive shear stress (τ) relates to the relative displacement, between the adhesive-inner adherend interface and adhesive-outer adherend interface, as:

$$\tau_a=G_a\frac{u_{oa}-u_{ia}}{t_a}. \tag{19}$$

Substituting Eqs. (7), (14) and (19) in Eq. (17), and evaluating the integral in the right hand of Eq. (17) leads to:

$$E_i\left(R_it_i\frac{\partial^2 u_{ia}}{\partial x^2}+\frac{(r_i^3-R_it_i^2)G_a}{2t_aG_i}\left(\frac{\partial^2 u_{oa}}{\partial x^2}-\frac{\partial^2 u_{ia}}{\partial x^2}\right)\right)+R_aG_a\frac{u_{oa}-u_{ia}}{t_a}=\rho_i\left(R_it_i\frac{\partial^2 u_{ia}}{\partial t^2}+\frac{(r_i^3-R_it_i^2)G_a}{2t_aG_i}\left(\frac{\partial^2 u_{oa}}{\partial t^2}-\frac{\partial^2 u_{ia}}{\partial t^2}\right)\right), \tag{20}$$

Likewise, substituting Eqs. (8), (16) and (19) in Eq. (18), and evaluating the integral in the right hand of Eq. (18) yields:

$$E_o\left(R_ot_o\frac{\partial^2 u_{oa}}{\partial x^2}-\frac{(r_o^3-R_ot_o^2)G_a}{2t_aG_o}\left(\frac{\partial^2 u_{oa}}{\partial x^2}-\frac{\partial^2 u_{ia}}{\partial x^2}\right)\right)-R_aG_a\frac{u_{oa}-u_{ia}}{t_a}=\rho_o\left(R_ot_o\frac{\partial^2 u_{oa}}{\partial t^2}-\frac{(r_o^3-R_ot_o^2)G_a}{2t_aG_o}\left(\frac{\partial^2 u_{oa}}{\partial t^2}-\frac{\partial^2 u_{ia}}{\partial t^2}\right)\right). \tag{21}$$

Equations (20) and (21) represent a coupled system of linear partial differential equations that govern the dynamic axial response of the overlap region in the tubular adhesive joint. These equations are formulated in terms of the interfacial axial displacements—u_{ia} for the inner adherend and u_{oa} for the outer adherend—which describe the relative motion across the bonded surfaces.

Once the interfacial displacement fields u_{ia} and u_{oa} are determined, the shear stress distribution within the adhesive layer can be directly evaluated. This provides critical insight into the load transfer mechanism across the bonded interface. Subsequently, other key mechanical quantities—such as the axial forces within the adherends and their corresponding axial displacements—can be derived from the displacement and stress fields. This stepwise analytical framework facilitates a comprehensive understanding of the joint's structural response under dynamic loading conditions.

2.2. Harmonic solutions

In this section, we aim to solve Eqs. (20) and (21) under the effect of a harmonic load $P(t)=Re\left(\tilde{P}e^{i\omega t}\right)$, uniformly applied to the right end of the inner tube, as illustrated in Figs. 5 and 6. To facilitate this analysis, the interfacial displacements u_{ia} and u_{oa} are also assumed harmonic. Accordingly, they are expressed as:

$$u_{ia}(x,t)=Re(U_{ia}e^{i(\xi x+\omega t)})=Re\left(\tilde{U}_{ia}e^{i\omega t}\right) \tag{22}$$

and,

$$u_{oa}(x,t)=Re(U_{oa}e^{i(\xi x+\omega t)})=Re\left(\tilde{U}_{oa}e^{i\omega t}\right). \tag{23}$$

where $\left(\tilde{U}_{ia}=U_{ia}e^{i\xi x}\right)$ and $\left(\tilde{U}_{oa}=U_{oa}e^{i\xi x}\right)$ are the complex magnitude of the displacements at the adhesive-adherends interfaces, ξ is the spatial wavenumber and ω is the angular frequency.

Substituting these expressions into Eqs. (20) and (21), and using the harmonic time dependency, the equations reduce to the following algebraic system:

$$\left(\frac{\rho_i\omega^2}{E_i}-\xi^2\right)\left(R_it_iU_{ia}+\frac{(r_i^3-R_it_i^2)G_a}{2t_aG_i}(U_{oa}-U_{ia})\right)+\frac{R_aG_a}{E_it_a}(U_{oa}-U_{ia})=0, \tag{24}$$

and,

$$\left(\frac{\rho_o\omega^2}{E_o}-\xi^2\right)\left(R_ot_oU_{oa}-\frac{(r_o^3-R_ot_o^2)G_a}{2t_aG_o}(U_{oa}-U_{ia})\right)-\frac{R_aG_a}{E_ot_a}(U_{oa}-U_{ia})=0. \tag{25}$$

For clarity in the subsequent derivations, we introduce the following parameters:

$$\alpha_i=\frac{(r_i^3-R_it_i^2)G_a}{2G_iR_it_it_a}, \tag{26}$$

$$\alpha_o=\frac{(r_o^3-R_ot_o^2)G_a}{2G_oR_ot_ot_a}, \tag{27}$$

$$\beta_i=\frac{R_aG_a}{E_iR_it_it_a}, \tag{28}$$

and,

$$\beta_o=\frac{R_aG_a}{E_oR_ot_ot_a}. \tag{29}$$

Introducing the wavenumbers $\left(k_i=\omega/\sqrt{E_i/\rho_i}\right)$ and $\left(k_o=\omega/\sqrt{E_o/\rho_o}\right)$ for the free parts of the inner and outer tubes, respectively, Eqs. (24) and (25) can be rewritten in a compact form as:

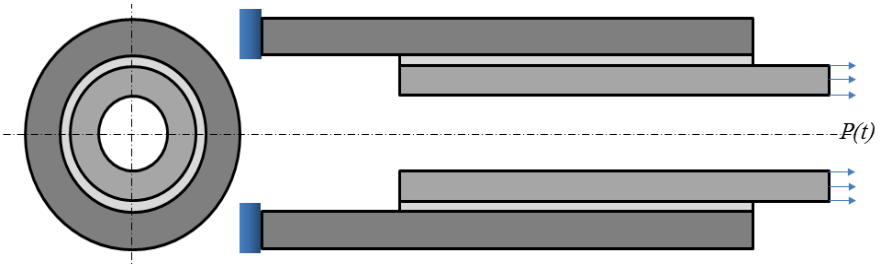


Fig 5. Boundary conditions.



Fig. 6. Boundary conditions using sub-structure technique.

$$(k_i^2\text{-}\xi^2)(U_{ia}+\alpha_i(U_{oa}\text{-}U_{ia}))+\beta_i(U_{oa}\text{-}U_{ia})=0, \tag{30}$$

and,

$$(k_o^2\text{-}\xi^2)(U_{oa}\text{-}\alpha_o(U_{oa}\text{-}U_{ia}))\text{-}\beta_o(U_{oa}\text{-}U_{ia})=0, \tag{31}$$

These two coupled algebraic equations describe the axial harmonic response of the tubular adhesive joint in terms of the complex displacement amplitudes at the interfaces. They form the basis for evaluating natural frequencies and adhesive shear stress distribution.

By rewriting Eqs. (30) and (31) in matrix form, we obtain the following system of linear equations:

$$\begin{bmatrix}(1\text{-}\alpha_i)(k_i^2\text{-}\xi^2)\text{-}\beta_i & \alpha_i(k_i^2\text{-}\xi^2)+\beta_i \\ \alpha_o(k_o^2\text{-}\xi^2)+\beta_o & (1\text{-}\alpha_o)(k_o^2\text{-}\xi^2)\text{-}\beta_o\end{bmatrix}\begin{pmatrix}U_{ia}\\ U_{oa}\end{pmatrix}=\begin{pmatrix}0\\0\end{pmatrix}. \tag{32}$$

To ensure non-trivial solutions for the displacement amplitudes U_{ia} and U_{oa}, the determinant of the coefficient matrix must be set to zero. This condition leads to the following characteristic equation:

$$\Big((1\text{-}\alpha_i)(k_i^2\text{-}\xi^2)\text{-}\beta_i\Big)\Big((1\text{-}\alpha_o)(k_o^2\text{-}\xi^2)\text{-}\beta_o\Big)\text{-}(\alpha_i(k_i^2\text{-}\xi^2)+\beta_i)(\alpha_o(k_o^2\text{-}\xi^2)+\beta_o)=0. \tag{33}$$

Equation (33) can be further simplified into a quadratic form with respect to ξ^2:

$$a\xi^4+b\xi^2+c=0, \tag{34}$$

where the coefficients a, b, and c are defined as:

$$a=1\text{-}\alpha_i\text{-}\alpha_o, \tag{35}$$

$$b=\text{-}a(k_i^2+k_o^2)+(\beta_i+\beta_o), \tag{36}$$

$$c=ak_i^2k_o^2\text{-}(\beta_ik_o^2+\beta_ok_i^2). \tag{37}$$

The general solution of Eq. (34) yields four values of ξ, corresponding to wave propagation in both directions for each mode:

$$\left\{\sqrt{\frac{\text{-}b+\sqrt{d}}{2a}},\text{-}\sqrt{\frac{\text{-}b+\sqrt{d}}{2a}},\sqrt{\frac{\text{-}b\text{-}\sqrt{d}}{2a}},\text{-}\sqrt{\frac{\text{-}b\text{-}\sqrt{d}}{2a}}\right\}. \tag{38}$$

where the discriminant d is given by:

$$d=b^2\text{-}4ac=a^2(\xi_i^2\text{-}\xi_o^2)^2+(\beta_i+\beta_o)^2\text{-}2a(\beta_i\text{-}\beta_o)(\xi_i^2\text{-}\xi_o^2), \tag{39}$$

Let us define the two positive wavenumbers $\xi_1=\sqrt{\frac{\text{-}b+\sqrt{d}}{2a}}$ and $\xi_2=\sqrt{\frac{\text{-}b\text{-}\sqrt{d}}{2a}}$. Then, the complex amplitudes of the interfacial displacements can be expressed as:

$$\tilde{U}_{ia}=(Ae^{\text{-}i\xi_1x}+Be^{i\xi_1x})+(Ce^{\text{-}i\xi_2x}+De^{i\xi_2x}), \tag{40}$$

and,

$$\tilde{U}_{oa}=\varphi_1(Ae^{\text{-}i\xi_1x}+Be^{i\xi_1x})+\varphi_2(Ce^{\text{-}i\xi_2x}+De^{i\xi_2x}), \tag{41}$$

with the coefficients φ_1 and φ_2 are given by:

$$\varphi_1=\text{-}\frac{(1\text{-}\alpha_i)(k_i^2\text{-}\xi_1^2)\text{-}\beta_i}{\alpha_i(k_i^2\text{-}\xi_1^2)+\beta_i}, \tag{42}$$

and,

$$\varphi_2=-\frac{(1-\alpha_i)(k_i^2-\xi_2^2)-\beta_i}{\alpha_i(k_i^2-\xi_2^2)+\beta_i}. \tag{43}$$

These expressions provide the general form of the harmonic displacement fields at the adhesive interfaces and serve as the basis for constructing the complete dynamic solution, subject to appropriate boundary and continuity conditions.

Substituting Eqs. (40) and (41) into Eq. (14), the complex magnitude of the normal force in the inner adherend is expressed as:

$$\tilde{N}_i=E_iS_i\left(i\xi_1p_{i1}(-Ae^{-i\xi_1x}+Be^{i\xi_1x})+i\xi_2p_{i2}(-Ce^{-i\xi_2x}+De^{i\xi_2x})\right). \tag{44}$$

where,

$$p_{i1}=1+\alpha_i(\varphi_1-1), \tag{45}$$

$$p_{i2}=1+\alpha_i(\varphi_2-1). \tag{46}$$

Likewise, substituting Eqs. (40) and (41) into Eqs. (16), the normal force in the outer adherend is given by:

$$\tilde{N}_o=E_oS_o\left(i\xi_1p_{o1}(-Ae^{-i\xi_1x}+Be^{i\xi_1x})+i\xi_2p_{o2}(-Ce^{-i\xi_2x}+De^{i\xi_2x})\right), \tag{47}$$

where,

$$p_{o1}=\varphi_1-\alpha_o(\varphi_1-1), \tag{48}$$

$$p_{o2}=\varphi_2-\alpha_o(\varphi_2-1). \tag{49}$$

To express the boundary conditions in the following section, it is also necessary to derive the average displacements over the cross-section of the adherends. These are obtained by integrating the axial displacement through the tube thickness and dividing by the cross-sectional area. For the inner tube, the average displacement is:

$$\langle u_i\rangle(x,t)=\frac{2\pi\int_0^{t_i}u_i(x,r,t)\ rdr}{\pi(R_I^2-R_{II}^2)}=u_{ia}(x,t)+\alpha_i(u_{oa}(x,t)-u_{ia}(x,t)), \tag{50}$$

and the average displacement in the outer tube is:

$$\langle u_o\rangle(x,t)=\frac{2\pi\int_0^{t_o}u_o(x,r,t)\ rdr}{\pi(R_{IV}^2-R_{III}^2)}=u_{oa}(x,t)-\alpha_o\left(u_{oa}(x,t)-u_{ia}(x,t)\right). \tag{51}$$

Substituting Eqs. (40) and (41) into Eqs. (50) and (51), the expressions for the average interfacial displacements of the inner and outer adherends become:

$$\langle\tilde{U}_i\rangle=p_{i1}(Ae^{-i\xi_1x}+Be^{i\xi_1x})+p_{i2}(Ce^{-i\xi_2x}+De^{i\xi_2x}), \tag{52}$$

and,

$$\langle\tilde{U}_o\rangle=p_{o1}(Ae^{-i\xi_1x}+Be^{i\xi_1x})+p_{o2}(Ce^{-i\xi_2x}+De^{i\xi_2x}). \tag{53}$$

2.3. Boundary conditions

The general boundary conditions for the tubular adhesive joint are illustrated in Fig. 5. Specifically, the outer tube is clamped at its left end, while the inner tube is subjected to an external harmonic axial load $P(t)$ applied at its right end. The boundary conditions were selected to ensure the correct dynamic response of the tubular joint. At the left side, a fixed boundary is applied to prevent rigid body motions. At the right side, a harmonic load is prescribed to excite the structure and obtain its harmonic response, allowing the identification of the natural frequencies of the joint.

To model the dynamic response of the system, the joint is conceptually divided into three distinct regions (see Fig. 6): the central overlap region, the left region, which consists solely of the outer tube, and the right region, which contains only the inner tube.

In the central region, the displacement field is represented by a superposition of four wave components (with amplitudes A, B, C and D), corresponding to forward and backward traveling waves for each of the two distinct wavenumbers. In contrast, wave propagation in the left and right regions is purely axial.

In the left region, two axial waves (A_l and B_l) travel in opposite directions at a wave speed v_o. Consequently, the complex magnitudes of the axial displacement and axial force in the outer tube within this region can be expressed as:

$$\tilde{U}_l=A_le^{-ik_ox}+B_le^{ik_ox}. \tag{54}$$

and,

$$\tilde{N}_l=ik_oE_oS_o(-A_le^{-ik_ox}+B_le^{ik_ox}), \tag{55}$$

Likewise, let A_r and B_r denote the amplitudes of the two axial waves in the right region, both propagating at the wave speed v_i. The axial complex magnitudes of the displacement and the axial force in the inner tube within this region are then expressed as:

$$\tilde{U}_r=A_re^{-ik_ix}+B_re^{ik_ix}. \tag{56}$$

and,

$$\tilde{N}_r=ik_iE_iS_i(-A_re^{-ik_ix}+B_re^{ik_ix}), \tag{57}$$

To determine the eight frequency-dependent coefficients — A, B, C, D, A_l, B_l, A_r and B_r — it is necessary to establish a system of eight independent equations. These equations can be formulated by applying appropriate boundary and continuity conditions. Specifically, they arise from the clamped boundary condition at the end of the outer tube, the external harmonic axial load applied



to the inner tube, and the conditions of continuity for both axial displacements and axial forces at the interfaces between the three regions. Together, these constraints ensure a physically consistent and mathematically solvable problem formulation for the dynamic behavior of the system.

First, the left end of the outer tube is clamped, which imposes a zero-displacement boundary condition. This yields:

$$\tilde{U}_l(x_l=0)=A_l+B_l=0. \tag{58}$$

Second, both the axial displacement and axial force must remain continuous at the interface between the left region and the overlapping region. This continuity leads to the following conditions:

$$\tilde{U}_l(x_l=l_l)=\langle\tilde{U}_{oa}\rangle(x=0). \tag{59}$$

and,

$$\tilde{N}_l(x_l=l_l)=\tilde{N}_o(x=0). \tag{60}$$

By substituting Eqs. (47) and (53) into the above continuity conditions, we obtain the following expressions:

$$A_l e^{-ik_o l_l}+B_l e^{ik_o l_l}-p_{o1}(A+B)-p_{o2}(C+D)=0. \tag{61}$$

and,

$$-A_l e^{-ik_o l_l}+B_l e^{ik_o l_l}-\frac{\xi_1 p_{o1}}{k_o}(-A+B)-\frac{\xi_2 p_{o2}}{k_o}(-C+D). \tag{62}$$

Furthermore, the boundary conditions at the free ends must also be satisfied. At the left end of the inner tube and the right end of the outer tube, the normal forces vanish due to the free-end conditions:

$$\tilde{N}_i(x=0)=0, \tag{63}$$

and,

$$\tilde{N}_o(x=l_0)=0. \tag{64}$$

By substituting Eqs. (44) and (47) into the free-end boundary conditions given in Eqs. (63) and (64), we obtain two additional relations for the unknown coefficients:

$$p_{i1}(-A+B)+\frac{\xi_2 p_{i2}}{\xi_1}(-C+D)=0 \tag{65}$$

and,

$$p_{o1}(-Ae^{-i\xi_1 l_0}+Be^{i\xi_1 l_0})+\frac{\xi_2 p_{i2}}{\xi_1}(-Ce^{-i\xi_2 l_0}+De^{i\xi_2 l_0}). \tag{66}$$

Moreover, continuity of axial displacement and axial force must also be enforced at the interface between the central region and the right region. These continuity conditions are expressed as:

$$\tilde{U}_r(x_r=0)=\langle\tilde{U}_i\rangle(x=l_0). \tag{67}$$

and,

$$\tilde{N}_r(x_r=0)=\tilde{N}_i(x=l_0). \tag{68}$$

Substituting Eqs. (44) and (52) into Eqs. (67) and (68), we obtain the following equations:

$$A_r+B_r-p_{i1}(Ae^{-i\xi_1 l_0}+Be^{i\xi_1 l_0})-p_{i2}(Ce^{-i\xi_2 l_0}+De^{i\xi_2 l_0})=0 \tag{69}$$

and,

$$-A_r+B_r-\frac{\xi_1 p_{i1}}{k_i}(-Ae^{-i\xi_1 l_0}+Be^{i\xi_1 l_0})-\frac{\xi_2 p_{i2}}{k_i}(-Ce^{-i\xi_2 l_0}+De^{i\xi_2 l_0})=0. \tag{70}$$

Finally, the right end of the inner tube is subjected to an external harmonic axial load $\tilde{P}$. This condition is expressed as:

$$\tilde{N}_r(x_r=l_r)=\tilde{P}. \tag{71}$$

which, when expressed in terms of wave components, becomes:

$$-A_r e^{-i\xi_i l_r}+B_r e^{i\xi_i l_r}=\frac{\tilde{P}}{ik_i E_i S_i}. \tag{72}$$

By assembling Eqs. (58), (61), (62), (65), (66), (69), (70), and (72), we obtain the following matrix system governing the unknown wave amplitudes A, B, C, D, A_l, B_l, A_r and B_r:

$$\begin{bmatrix}
0 & 0 & 0 & 0 & 1 & 1 & 0 & 0\\
-p_{o1} & -p_{o1} & -p_{o2} & -p_{o2} & e^{-ik_o l_l} & e^{ik_o l_l} & 0 & 0\\
\frac{\xi_1 p_{o1}}{k_o} & -\frac{\xi_1 p_{o1}}{k_o} & \frac{\xi_2 p_{o2}}{k_o} & -\frac{\xi_2 p_{o2}}{k_o} & -e^{-ik_o l_l} & e^{ik_o l_l} & 0 & 0\\
-p_{i1} & p_{i1} & -\frac{\xi_2 p_{i2}}{\xi_1} & \frac{\xi_2 p_{i2}}{\xi_1} & 0 & 0 & 0 & 0\\
-p_{o1}e^{-i\xi_1 l_0} & p_{o1}e^{i\xi_1 l_0} & -\frac{\xi_2 p_{i2}}{\xi_1}e^{-i\xi_2 l_0} & \frac{\xi_2 p_{i2}}{\xi_1}e^{i\xi_2 l_0} & 0 & 0 & 0 & 0\\
-p_{i1}e^{-i\xi_1 l_0} & -p_{i1}e^{i\xi_1 l_0} & -p_{i2}e^{-i\xi_2 l_0} & -p_{i2}e^{i\xi_2 l_0} & 0 & 0 & 1 & 1\\
\frac{\xi_1 p_{i1}}{k_i}e^{-i\xi_1 l_0} & -\frac{\xi_1 p_{i1}}{k_i}e^{i\xi_1 l_0} & \frac{\xi_2 p_{i2}}{k_i}e^{-i\xi_2 l_0} & -\frac{\xi_2 p_{i2}}{k_i}e^{i\xi_2 l_0} & 0 & 0 & -1 & 1\\
0 & 0 & 0 & 0 & 0 & 0 & -e^{-i\xi_i l_r} & e^{i\xi_i l_r}
\end{bmatrix}
\begin{bmatrix} A\\ B\\ C\\ D\\ A_l\\ B_l\\ A_r\\ B_r \end{bmatrix}
=
\begin{bmatrix} 0\\ 0\\ 0\\ 0\\ 0\\ 0\\ 0\\ \frac{\tilde{P}}{ik_i E_i S_i} \end{bmatrix}. \tag{73}$$

Solving the linear system in Eq. (73) yields the wave amplitudes A, B, C, D, A_l, B_l, A_r and B_r. The solution can be written as:

$$\begin{bmatrix} A \\ B \\ C \\ D \\ A_l \\ B_l \\ A_r \\ B_r \end{bmatrix} = \begin{bmatrix} 0 & 0 & 0 & 0 & 1 & 1 & 0 & 0 \\ -p_{o1} & -p_{o1} & -p_{o2} & -p_{o2} & e^{-ik_o l_l} & e^{ik_o l_l} & 0 & 0 \\ \frac{\xi_1 p_{o1}}{k_o} & -\frac{\xi_1 p_{o1}}{k_o} & \frac{\xi_2 p_{o2}}{k_o} & -\frac{\xi_2 p_{o2}}{k_o} & -e^{-ik_o l_l} & e^{ik_o l_l} & 0 & 0 \\ -p_{i1} & p_{i1} & -\frac{\xi_2 p_{i2}}{\xi_1} & \frac{\xi_2 p_{i2}}{\xi_1} & 0 & 0 & 0 & 0 \\ -p_{o1}e^{-i\xi_1 l_0} & p_{o1}e^{i\xi_1 l_0} & -\frac{\xi_2 p_{i2}}{\xi_1}e^{-i\xi_2 l_0} & \frac{\xi_2 p_{i2}}{\xi_1}e^{i\xi_2 l_0} & 0 & 0 & 0 & 0 \\ -p_{i1}e^{-i\xi_1 l_0} & -p_{i1}e^{i\xi_1 l_0} & -p_{i2}e^{-i\xi_2 l_0} & -p_{i2}e^{i\xi_2 l_0} & 0 & 0 & 1 & 1 \\ \frac{\xi_1 p_{i1}}{k_i}e^{-i\xi_1 l_0} & -\frac{\xi_1 p_{i1}}{k_i}e^{i\xi_1 l_0} & \frac{\xi_2 p_{i2}}{k_i}e^{-i\xi_2 l_0} & -\frac{\xi_2 p_{i2}}{k_i}e^{i\xi_2 l_0} & 0 & 0 & -1 & 1 \\ 0 & 0 & 0 & 0 & 0 & 0 & -e^{-i\xi_i l_r} & e^{i\xi_i l_r} \end{bmatrix}^{-1} \begin{bmatrix} 0 \\ 0 \\ 0 \\ 0 \\ 0 \\ 0 \\ 0 \\ \tilde{P} \\ \overline{ik_i E_i S_i} \end{bmatrix}. \tag{74}$$

Once the wave amplitudes are determined, various parameters within the overlap region can be computed. For example, using Eqs. (40) and (41), the amplitudes of the interfacial displacements $\tilde{U}_{ia}$ and $\tilde{U}_{oa}$ can be determined. Similarly, applying Eqs. (44) and (47), one can calculate the amplitudes of the normal forces $\tilde{N}_i$ and $\tilde{N}_o$.

Furthermore, using Eqs. (52) and (53), the average displacement amplitudes $\langle \tilde{U}_i \rangle$ and $\langle \tilde{U}_o \rangle$ can be obtained. Other key parameters, in the left and right regions, can also be evaluated. Specifically, the displacements and normal forces $\tilde{U}_l$, $\tilde{N}_l$, $\tilde{U}_r$ and $\tilde{N}_r$ can be computed using Eqs. (54), (55), (56), and (57), respectively.

As we are particularly interested in the harmonic response of the tubular adhesive joint, the transfer function is defined as the displacement at the point where the harmonic load is applied. According to Eq. (56), the transfer function is given by:

$$H = \tilde{U}_r(x = l_r) = A_r e^{-ik_i l_r} + B_r e^{ik_i l_r}. \tag{75}$$

In addition to the harmonic response, we are also interested in the shear stress distribution within the adhesive layer across the overlap region. Once the interfacial displacement amplitudes are known, the amplitude of the shear stress in the adhesive can be computed using:

$$\tilde{\tau}_a = \frac{G_a\left(\tilde{U}_{oa} - \tilde{U}_{ia}\right)}{t_a}, \tag{76}$$

or, equivalently,

$$\tilde{\tau}_a = \frac{G_a}{t_a}\left((\varphi_1 - 1)(Ae^{-i\xi_1 x} + Be^{i\xi_1 x}) + (\varphi_2 - 1)(Ce^{-i\xi_2 x} + De^{i\xi_2 x})\right), \tag{77}$$

The static shear stress distribution can be obtained by considering the limit as the frequency tends to zero.

3. Results and Discussion

3.1. Finite-element modelling

Numerical techniques have become increasingly prominent in solving complex engineering and mathematical problems. In this study, the finite element method (FEM) is employed using ANSYS to investigate the dynamic response of tubular adhesive joints under harmonic loading. The primary objective of the FEM analysis is to validate and compare the results obtained from the theoretical model.

For simplicity and due to geometric symmetry, a 2D axisymmetric model is used (see Fig. 7). Both the adherends and the adhesive layer are modeled as isotropic materials. The outer adherend is fixed at its left end, while a harmonic axial load is applied to the right end of the inner adherend. All tubular joint geometries, adhesive and adherend, were discretized using PLANE183 elements with the axisymmetric formulation enabled. The PLANE183 element is a higher-order, two-dimensional finite element featuring eight nodes and two translational degrees of freedom per node, corresponding to displacements in the x and y directions.

Six simulation cases are considered, using the same material properties as in the theoretical model. The corresponding geometrical and material parameters are summarized in Table 1. For each case, the distribution of shear stress within the adhesive layer and the frequency response are computed and compared to the analytical predictions presented in Section 3.2. In Case 1, both adherends are made of aluminum. The overlap length is set to 50 mm, and the free (non-overlapping) length of each adherend is 100 mm. The adhesive shear modulus is taken as 0.7 GPa. In Case 2, the adherends are changed to steel, while all other parameters remain unchanged. In Case 3 is identical to Case 1, except that the shear modulus of the adhesive is increased to 1 GPa. Cases 4 and 5 are designed to examine the effect of material asymmetry in the adherends. More precisely, the inner adherend is aluminum and the outer adherend is steel in Case 4, while, in Case 5, the configuration is reversed: the inner adherend is steel and the outer adherend is aluminum. In Case 6, the setup is the same as in Case 1, but the overlap length is reduced to 25 mm, allowing assessment of overlap length effects.

These six cases allow a comprehensive investigation of material contrast, adhesive stiffness, and geometric effects on the harmonic response of tubular adhesive joints. The FEM results serve to validate the accuracy and robustness of the proposed theoretical model.

A mesh convergence study was conducted for Case 1 to evaluate the sensitivity of the numerical solution to mesh discretization. The adhesive layer was initially discretized using a maximum element size of 1 mm, which was subsequently progressively refined in uniform increments of 0.1 mm. A total of ten successive refinement iterations were performed, during which the computed shear stress within the adhesive layer converged and ultimately stabilizing at a value around 276 Pa, as summarized in the (Table 2). A uniform mesh of size 0.25 mm was selected (Fig. 7) to mesh all layers as it is more than sufficient to catch the static and dynamic behaviors of the tubular joint.

Table 1. Geometrical and material parameters of the studied cases.

Case	1	2	3	4	5	6
$E_i\ (GPa)$	70	190	70	70	190	70
$E_o\ (GPa)$	70	190	70	190	70	70
$G_a\ (GPa)$	0.7	0.7	1	0.7	0.7	0.7
ν_i	0.34	0.29	0.34	0.34	0.29	0.34
ν_o	0.34	0.29	0.34	0.29	0.34	0.34
ν_a	0.4	0.4	0.4	0.4	0.4	0.4
$\rho_i\ (kg/m^3)$	2700	7850	2700	2700	7850	2700
$\rho_o\ (kg/m^3)$	2700	7850	2700	7850	2700	2700
$\rho_a\ (kg/m^3)$	1100	1100	1100	1100	1100	1100
$l_r, l_l (mm)$	100	100	100	100	100	100
$l_o\ (mm)$	50	50	50	50	50	25
$R_I\ (mm)$	15	15	15	15	15	15
$R_{II}\ (mm)$	19	19	19	19	19	19
$R_{III}\ (mm)$	20	20	20	20	20	20
$R_{IV}\ (mm)$	23.15	23.15	23.15	23.15	23.15	23.15

Table 2. Mesh convergence.

Iterations #	Mesh Size (mm)	Maximum Shear Stress (Pa)	% Error	Fundamental Frequency (Hz)	% Error
1	1	264.4271		5146.20	
2	0.9	274.6293	3.71	5142.83	0.066
3	0.8	288.7025	4.88	5141.65	0.004
4	0.7	278.7222	3.59	5141.89	0.005
5	0.6	277.7962	0.33	5141.50	0.007
6	0.5	277.6154	0.06	5141.67	0.003
7	0.4	277.5140	0.04	5141.19	0.009
8	0.3	277.4916	0.01	5141.31	0.002
9	0.2	277.4757	0.00	5141.00	0.006
10	0.1	277.3212	0.06	5141.48	0.009

Table 3: Comparison of theoretical and numerical natural frequencies

	1st natural frequency			2nd natural frequency			3rd natural frequency		
Case	Theory (kHz)	Finite-element (kHz)	***Error (%)***	Theory (kHz)	Finite-element (kHz)	***Error (%)***	Theory (kHz)	Finite-element (kHz)	***Error (%)***
1	4.73	5.14	**8.3**	14.34	17.04	**15.8**	24.27	27.16	**10.7**
2	4.46	4.74	**5.9**	13.45	15.86	**9.5**	22.56	24.34	**7.3**
3	4.75	5.18	**10.2**	14.44	17.20	**16.0**	24.46	27.38	**10.7**
4	6.00	6.42	**6.6**	12.89	15.14	**14.9**	24.00	26.18	**8.3**
5	3.20	3.46	**7.6**	14.97	16.84	**11.1**	23.00	25.28	**9.0**
6	5.29	5.76	**8.2**	15.88	18.46	**14.0**	26.48	29.82	**11.2**
Avg.			**7.8**			**13.5**			**9.5**

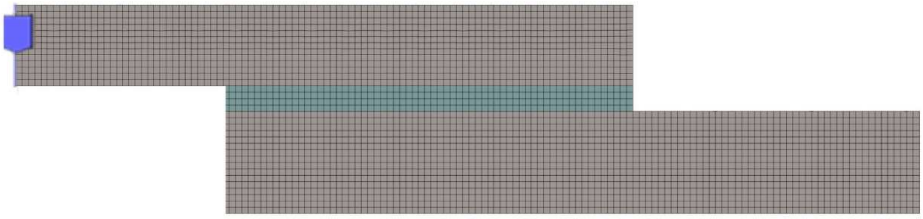


Fig. 7. Finite-element meshing of the tubular joint.

3.2. Validation and discussion

3.2.1. *Frequency response*

In this section, we focus on the frequency response of the tubular adhesive joint, which is defined as the axial displacement at the point of applied harmonic load. A comparison of the theoretical and numerical frequency responses is presented in Fig. 8 for the six different cases described earlier. Additionally, the first three natural frequencies obtained from both the theoretical model and finite element analysis (FEA), along with their relative errors, are summarized in Table 3.

Moreover, the present analysis neglects damping effects in order to preserve the clarity and analytical tractability of the proposed model. Nevertheless, the formulation can be readily extended to account for damping by adopting a complex-valued representation of the Young's and shear moduli, following the approach proposed by Almitani and Othman [34] for double-lap joints.

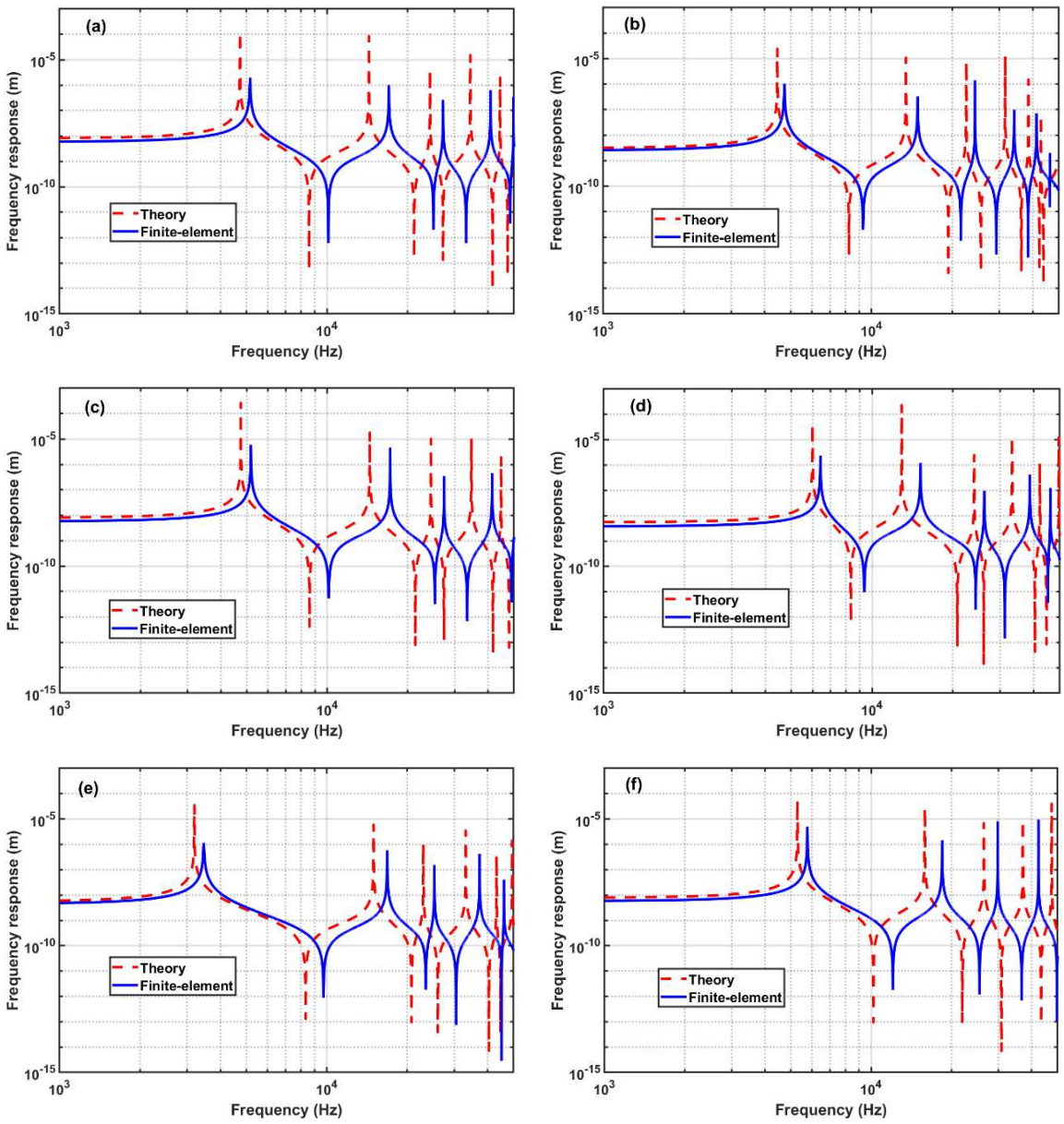


Fig. 8. Frequency responses: (a) Case 1, (b) Case 2, (c) Case 3, (d) Case 4, (e) Case 5, and (f) Case 6.

In the case of tubular joints, however, the governing equations are inherently more complex, and the introduction of complex material properties would considerably increase the mathematical complexity without providing significant additional insight into the location of the natural frequencies. It is worth noting that damping primarily affects vibration amplitudes and has only a limited influence on the position of natural frequencies, particularly when the damping ratio is below 0.1, as discussed in [34]. Consequently, the undamped natural frequencies reported herein remain representative of the fundamental dynamic characteristics of the system.

Across all six cases, the theoretical model exhibits a similar trend to the FEA results, demonstrating consistent qualitative agreement. However, some discrepancies are observed. In particular, the theoretical model systematically underestimates the natural frequencies when compared to the numerical predictions. This underestimation is primarily attributed to the fact that the theoretical model yields a lower overall stiffness for the tubular joint assembly than the FEM model. This stiffness discrepancy is further corroborated by the observation of slightly larger static deflections predicted by the theoretical approach in all six cases. Despite these differences, the theoretical model captures the essential dynamic behavior of the system and remains a valuable tool for preliminary design and parameter studies, especially when computational efficiency is a concern.

The errors in the first natural frequency are the lowest among the three modes, ranging from 5.9% to 10.2%, with an average value of 7.8%. In contrast, the second natural frequency exhibits the highest discrepancies, with errors ranging from 9.5% to 16% and an average error of 13.5%. The third natural frequency shows intermediate deviations, with errors between 7.3% and 11.2%, resulting in an average value of 9.5%.

Among the six cases studied, Case 2—in which both adherends are made of steel—shows the lowest overall errors. The second- and third-lowest errors are observed in Cases 4 and 5, respectively, where the structure includes a combination of steel and aluminum adherends. Conversely, the largest errors are seen in Case 3, where the shear modulus of the adhesive is increased from 0.7 GPa to 1 GPa. Interestingly, Case 6, with a shorter overlap length (25 mm instead of 50 mm), yields smaller errors than Case 1, suggesting that the overlap length has a secondary influence compared to material stiffness.

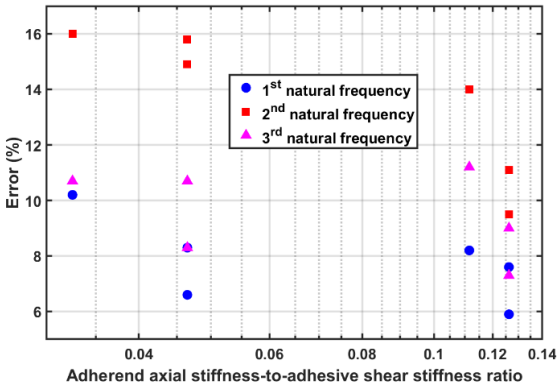


Fig. 9. Effect of axial adherend stiffness-to-shear adhesive stiffness ratio on the errors on the natural frequencies.

This analysis reveals a clear trend: as the axial stiffness of the adherends increases, the errors on the predicted natural frequencies decrease. This explains why Case 2, with the highest axial stiffness, exhibits the best agreement with FEM results. Similarly, the good performance of Cases 4 and 5 can be attributed to their partially stiff adherends. Moreover, increasing the shear stiffness of the adhesive layer results in larger errors, as observed in Case 3. This highlights the sensitivity of the theoretical model to the stiffness contrast between the adhesive and the adherends.

In conclusion, the accuracy of the theoretical model is largely governed by the ratio of axial stiffness of the adherends to the shear stiffness of the adhesive. A higher axial-to-shear stiffness ratio leads to better agreement with numerical predictions and lower errors in natural frequency estimation.

The effective axial inner adherend stiffness can be written as:

$$K_i = \frac{2\pi t_i R_i E_i}{(l_r + l_o)}, \tag{78}$$

and that of the outer adherend is expressed as:

$$K_o = \frac{2\pi t_o R_o E_o}{(l_l + l_o)}. \tag{79}$$

Meanwhile, the effective shear stiffness of the adhesive layer can be approximated by:

$$K_a = \frac{2\pi G_a l_o R_a}{t_a}. \tag{80}$$

Based on these expressions, the axial adherend stiffness-to-shear adhesive stiffness ratio is defined as:

$$K_r = \frac{K_i + K_o}{2K_a}. \tag{81}$$

Figure 9 presents the variation of the errors associated with the first three natural frequencies as a function of the stiffness ratio Kr. The plot clearly demonstrates that the errors decrease with increasing stiffness ratio. This trend can be interpreted by considering the assumptions of the theoretical model: as the axial stiffness of the adherends becomes much larger than the shear stiffness of the adhesive, the mechanical response tends toward one-dimensional kinematics, which aligns closely with the theoretical assumptions. Thus, the model becomes increasingly accurate in high-stiffness-ratio regimes.

3.2.2. Shear adhesive stress

Accurately predicting the distribution of shear stress within the adhesive layer is critical for evaluating the structural performance and durability of bonded tubular joints under dynamic loading. In this study, the theoretical model based on the linear radial shear stress assumption was used to estimate the adhesive shear stress distribution, and its predictions were compared to those obtained via detailed finite element simulations.

As illustrated in Fig. 10, a strong correlation is observed between the theoretical and finite element results across all six investigated cases. This validates the capability of the theoretical model to capture the key features of shear stress distribution along the overlap length. The agreement is particularly good in Case 2, where both adherends are made of steel. The high stiffness of the adherends in this configuration aligns well with the theoretical model's assumption of near-one-dimensional kinematics, thereby minimizing the influence of complex deformation modes and improving prediction accuracy. In numerical terms, the average difference in shear stress between theory and FEM in Case 2 is only 3.96%, and the peak stress differs by just 5.40%, confirming very strong alignment.

In contrast, Case 3, in which the shear modulus of the adhesive is increased from 0.7 GPa to 1 GPa, shows the largest deviations between the theoretical and FEM predictions. This outcome highlights the sensitivity of the model to adhesive shear stiffness: as the adhesive becomes stiffer relative to the adherends, the assumptions underlying the theoretical model—namely, that the adherends dominate the mechanical behavior and that the adhesive layer deforms in simple shear—become less valid, introducing complex stress distributions that the simplified model cannot fully capture. Quantitatively, Case 3 exhibits an average error of 14.3% and a maximum shear stress error of 17.3%, which is the highest among all cases and nearly four times larger than the error observed in Case 2.

Table 4 summarizes both the average shear stress error and the maximum shear stress prediction error for each case. The range of average errors spans from 3.96% to 14.3%, while peak stress deviations vary between 1.30% and 17.9%. The trend in errors clearly mirrors that seen in the natural frequency predictions, reinforcing the idea that the ratio of axial adherend stiffness to adhesive shear stiffness plays a fundamental role in determining the accuracy of the theoretical model. Notably, cases with stiffer adherends (Cases 1, 2, and 6) consistently remain below a 10% average error threshold, whereas cases with increased adhesive stiffness (Cases 3 and 5) exceed this threshold.

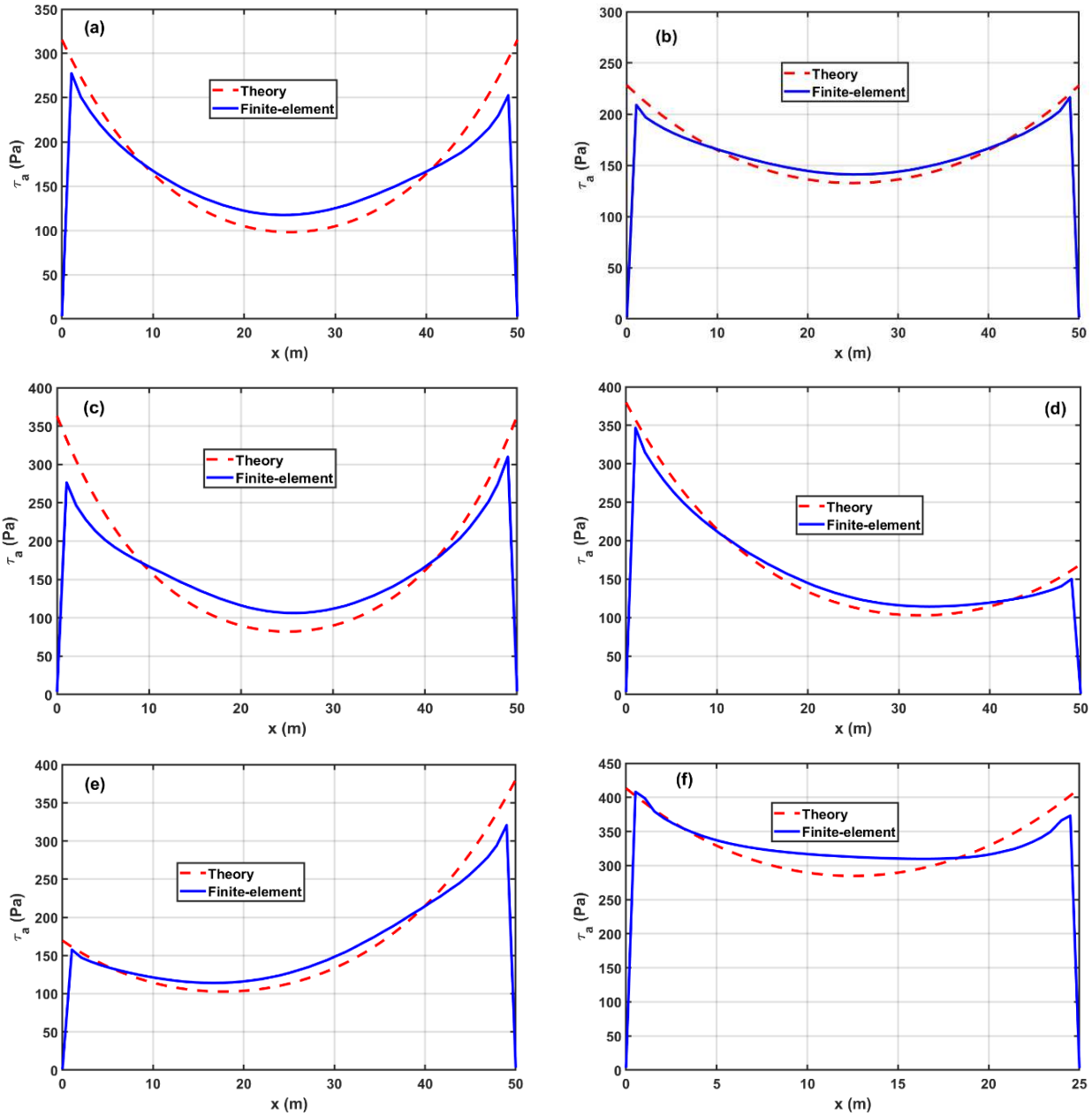


Fig. 10. Adhesive shear stress: (a) Case 1, (b) Case 2, (c) Case 3, (d) Case 4, (e) Case 5, and (f) Case 6.

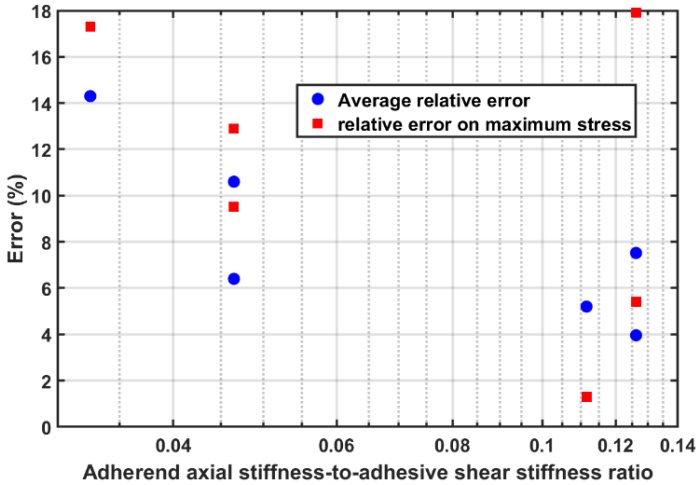


Fig. 11. Effect of axial adherend stiffness-to-shear adhesive stiffness ratio on the errors on the adhesive shear stress.

Table 4. Comparison of theoretical and numerical adhesive's shear stresses.

Case	Average overall *error (%)*	Maximum adhesive shear stress		
		Theory (Pa)	Finite-element (Pa)	*Error (%)*
1	**10.6**	313.2	277.5	**12.9**
2	**3.96**	228.2	216.5	**5.40**
3	**14.3**	363.1	310.0	**17.3**
4	**6.40**	379.7	346.7	**9.52**
5	**7.52**	378.1	320.7	**17.9**
6	**5.21**	413.4	408.1	**1.30**

This relationship is made explicit in Fig. 11, where the errors in shear stress prediction are plotted against the stiffness ratio Sr defined in Eq. (80). The plot shows a consistent decrease in error magnitude with increasing stiffness ratio. This finding confirms that a higher axial stiffness of the adherends relative to the adhesive layer leads to a mechanical behavior that is more accurately described by the assumptions of the analytical model. In such cases, the deformation of the system is predominantly axial, and the adhesive layer is primarily subjected to uniform shear, which aligns well with the theoretical formulation.

In summary, the findings in this section underline the importance of the adherend-to-adhesive stiffness ratio in determining both the stress distribution accuracy and the dynamic response prediction of tubular adhesive joints. The theoretical model proves to be robust and reliable in scenarios where the stiffness contrast is large. However, for configurations with low stiffness contrast, caution must be exercised, and complementary numerical methods may be required to ensure accurate design predictions. Overall, the quantitative comparison shows that the theoretical model predicts shear stresses within a 4–10% error range under favorable stiffness conditions but may deviate by up to 17–18% when adhesive stiffness becomes dominant.

5. Conclusion

In this study, a theoretical model was developed to predict the dynamic axial response and shear stress distribution in tubular adhesive joints, based on the assumption of a linear variation of adhesive shear stress with radial coordinate. The model was formulated using elasticity theory and validated against finite element simulations using a 2D axisymmetric approach in ANSYS. The focus was placed on evaluating the model's accuracy in predicting both natural frequencies and adhesive shear stresses under harmonic loading. A total of six cases were examined to investigate the effects of material properties (aluminum vs. steel adherends), adhesive stiffness, and overlap length. The theoretical predictions were found to be in good agreement with the numerical results. The first natural frequency was consistently predicted with the lowest error, while the second mode showed the highest discrepancies. Importantly, a clear correlation was established between the model's accuracy and the axial adherend stiffness-to-shear adhesive stiffness ratio. Higher values of this ratio resulted in lower prediction errors for both natural frequencies and adhesive shear stress, confirming the suitability of the theoretical assumptions under such conditions.

Author Contributions

Author 1 planned the scheme, initiated the project, and suggested the experiments; Author 2 conducted the experiments and analyzed the empirical results; Author 3 developed the mathematical modeling and examined the theory validation. The manuscript was written through the contribution of all authors. All authors discussed the results, reviewed, and approved the final version of the manuscript.

Acknowledgments

Not applicable.

Conflict of Interest

The authors declared no potential conflicts of interest concerning the research, authorship, and publication of this article.

Funding

The authors received no financial support for the research, authorship, and publication of this article.

Data Availability Statements

The datasets generated and/or analyzed during the current study are available from the corresponding author on reasonable request.

Nomenclature

Coordinates, time and frequency

x Axial coordinate
r Radial coordinate
t Time
ω Angular frequency

Geometrical parameters

ε_o Normal/axial in the outer tube
γ_a Shear strain in the adhesive
γ_i Shear strain in the inner tube
γ_o Shear strain in the outer tube

Stresses

σ_i Normal/axial stress in the inner tube

R_I	Inner radius of the inner tube
R_{II}	Outer radius of the inner tube
R_{III}	Inner radius of the outer tube
R_{IV}	Outer radius of the outer tube
$R_i=\frac{R_I+R_{II}}{2}$	Radius at mid-thickness of the inner tube
$R_o=\frac{R_{III}+R_{IV}}{2}$	Radius at mid-thickness of the outer tube
$R_a=\frac{R_{II}+R_{III}}{2}$	Radius at mid-thickness of the adhesive layer
$t_i=R_{II}$-R_I	Thickness of the inner tube
$t_o=R_{IV}$-R_{III}	Thickness of the outer tube
$t_a=R_{III}$-R_{II}	Thickness of the adhesive layer
S_i	Cross-sectional area of the inner tube
S_o	Cross-sectional area of the outer tube
l_0	Length of the overlap region
l_l	Length of the left region
l_r	Length of the right region

Material parameters

G_a	Shear modulus of the adhesive
G_i	Shear modulus of the inner tube
G_o	Shear modulus of the outer tube
E_i	Young's modulus of the inner tube
E_o	Young's modulus of the outer tube
ρ_i	Density of the inner tube
ρ_o	Density of the outer tube
ν_a	Poisson's ratio of the adhesive
ν_i	Poisson's ratio of the inner tube
ν_o	Poisson's ratio of the outer tube

Displacements

u_i	Axial displacement of the inner tube
u_o	Axial displacement of outer tube
$\langle u_i \rangle$	Average axial displacement of the inner tube
$\langle u_o \rangle$	Average axial displacement of the outer tube
u_{ia}	Axial displacement at the interface between the inner tube and the adhesive $(u_{ia}(x)=u_i(x,r=R_{II}))$
u_{oa}	Axial displacement at the interface between the outer tube and the adhesive $(u_{oa}(x)=u_o(x,r=R_{III}))$

σ_o	Normal/axial stress in the outer tube
τ_a	Shear stress in the adhesive
τ_i	Shear stress in the inner tube
τ_o	Shear stress in the outer tube
$\tilde{\tau}_a$	Complex magnitude of the shear stress in the adhesive

Forces

N_i	Normal/axial force in the inner tube
N_o	Normal/axial force in the outer tube
$\tilde{N}_i$	Complex magnitude of the axial force in the inner tube
$\tilde{N}_o$	Complex magnitude of the axial force in the outer tube
$\tilde{N}_l$	Complex magnitude of the axial force in the outer tube at the left region
$\tilde{N}_r$	Complex magnitude of the axial force in the inner tube at the right region

Additional constants

$r_i=\sqrt[3]{\frac{R_I^3+R_I^2R_{II}-5R_IR_{II}^2+3R_{II}^2}{12}}$	Characteristic radius of the inner tube
$r_o=\sqrt[3]{\frac{R_{IV}^3+R_{IV}^2R_{III}-5R_{IV}R_{III}^2+3R_{III}^2}{12}}$	Characteristic radius of the outer tube
$v_i=\sqrt{\frac{E_i}{\rho_i}}$	Wave speed in the inner tube
$v_o=\sqrt{\frac{E_o}{\rho_o}}$	Wave speed in the outer tube
$k_i=\frac{\omega}{v_i}$	Wavenumber of the inner tube
$k_o=\frac{\omega}{v_o}$	Wavenumber of the outer tube
A, B, C, D	Amplitude of waves in the overlap region
A_l and B_l	Amplitude of waves in the left region
A_r and B_r	Amplitude of waves in the right region
K_i	Effective axial inner adherend stiffness
K_o	Effective axial outer adherend stiffness
K_a	Effective shear adhesive stiffness
K_r	Axial adherend stiffness-to-shear adhesive stiffness ratio

More constants used for sake of simplicity

$$\alpha_i=\frac{(r_i^3-R_it_i^2)G_a}{2G_iR_it_it_a}$$

$$\alpha_o=\frac{(r_o^3-R_ot_o^2)G_a}{2G_oR_ot_ot_a}$$

$$\beta_i=\frac{R_aG_a}{E_iR_it_it_a}$$

$$\beta_o=\frac{R_aG_a}{E_oR_ot_ot_a}$$

$$a=1-\alpha_i-\alpha_o$$

$$b=-a(k_i^2+k_o^2)+(\beta_i+\beta_o)$$

$\langle \tilde{U}_i \rangle$	Complex magnitude of the average axial displacement of the inner tube	$c=ak_i^2k_o^2-(\beta_ik_o^2+\beta_ok_i^2)$
$\langle \tilde{U}_o \rangle$	Complex magnitude of the average axial displacement of the outer tube	$\xi_1=\left(\frac{-b+(b^2-4ac)^{\frac{1}{2}}}{2a}\right)^{\frac{1}{2}}$
$\tilde{U}_{ia}=U_{ia}e^{i\xi x}$	Complex magnitude of the axial displacement at the interface between the inner tube and the adhesive	$\xi_2=\left(\frac{b+(b^2-4ac)^{\frac{1}{2}}}{2a}\right)^{\frac{1}{2}}$
$\tilde{U}_{io}=U_{io}e^{i\xi x}$	Complex magnitude of the axial displacement at the interface between the outer tube and the adhesive	$\varphi_1=-\frac{(1-\alpha_i)(k_i^2-\xi_1^2)-\beta_i}{\alpha_i(k_i^2-\xi_1^2)+\beta_i}$
$\tilde{U}_l$	Complex magnitude of the axial displacement in the outer tube at the left region	$\varphi_2=-\frac{(1-\alpha_i)(k_i^2-\xi_2^2)-\beta_i}{\alpha_i(k_i^2-\xi_2^2)+\beta_i}$
$\tilde{U}_r$	Complex magnitude of the axial displacement in the inner tube at the right region	$p_{i1}=1+\alpha_i(\varphi_1-1)$
H	Transfer function	$p_{i2}=1+\alpha_i(\varphi_2-1)$
	Strains	$p_{o1}=\varphi_1-\alpha_o(\varphi_1-1)$
ε_i	Normal/axial strain in the inner tube	$p_{o2}=\varphi_2-\alpha_o(\varphi_2-1)$

References

[1] Zhang, T., Zhang, Y., Jiang, K., Research on Adhesion Pull-Off Behavior of Rigid Flat Punch and Viscoelastic Substrate, *Mathematics*, 12, 2024, 3454.
[2] Wei, H., Li, Y., Xun, Y., Zhong, H., Theoretical and Experimental Vibration Generation in a Coaxial Pulse-Tube Cryocooler, *Vibration*, 7, 2024, 1226–1247.
[3] Gantes, C.J., Vernardos, S.M., Koulatsou, K.G., Gül, S., Nonlinear Finite Element Analysis of Tubular Steel Wind Turbine Towers near Man Door and Ventilation Openings to Optimize Design against Buckling, *Vibration*, 7, 2024, 212–228.
[4] Kondakcı, K., Coskun, S.B., Analysis of the Axial Vibration of Non-Uniform and Functionally Graded Rods via an Analytical-Based Numerical Approach, *Vibration*, 6, 2023, 876–894.
[5] Dragoni, E., Goglio, L., Adhesive stresses in axially-loaded tubular bonded joints - Part I: Critical review and finite element assessment of published models, *International Journal of Adhesion and Adhesives*, 47, 2013, 35–45.
[6] Goglio, L., Paolino, D.S., Adhesive stresses in axially-loaded tubular bonded joints - Part II: Development of an explicit closed-form solution for the Lubkin and Reissner model, *International Journal of Adhesion and Adhesives*, 48, 2014, 35–42.
[7] Kumar, S., Khan, M., A shear-lag model for functionally graded adhesive anchors, *International Journal of Adhesion and Adhesives*, 68, 2016, 317–325.
[8] Puigvert, F., Crocombe, A.D., Gil, L., Static analysis of adhesively bonded anchorages for CFRP tendons, *Construction and Building Materials*, 61, 2014, 206–215.
[9] Wu, C., He, L., Ghafoori, E., Zhao, X.L., Torsional strengthening of steel circular hollow sections (CHS) using CFRP composites, *Engineering Structures*, 171, 2018, 806–816.
[10] Othman, R., *Analytical modelling of dynamic and impact loads, In Strength Prediction of Adhesively-Bonded Joints*, CRC Press, 2017.
[11] Lubkin, J.L., Reissner, E., Stress distribution and design data for adhesive lap joints between circular tubes, *Transactions of the ASME – Journal of Fluids Engineering*, 78, 1956, 1213–1221.
[12] Goland, M., Reissner, E., The stresses in cemented joints, *Transactions of the ASME – Journal of Applied Mechanics*, 11, 1944, A17–27.
[13] Shi, Y.P., Cheng, S., Analysis of adhesive-bonded cylindrical lap joints subjected to axial load, *Journal of Engineering Mechanics*, 119, 1993, 584–602.
[14] Nemes, O., Lachaud, F., Mojtabi, A., Contribution to the study of cylindrical adhesive joining, *International Journal of Adhesion and Adhesives*, 26, 2006, 474–480.
[15] Nemes, O., Lachaud, F., Modeling of cylindrical adhesively bonded joints, *Journal of Adhesion Science and Technology*, 23, 2009, 1383–1393.
[16] Kumar, S., Analysis of tubular adhesive joints with a functionally modulus graded bondline subjected to axial loads, *International Journal of Adhesion and Adhesives*, 29, 2009, 785–795.
[17] Kumar, S., Scanlan, J.P., Stress analysis of shaft-tube bonded joints using a variational method, *Journal of Adhesion*, 86, 2010, 369–394.
[18] Martinez, M.A., Velasco, F., Abenojar, J., Pantoja, M., Del Real, J.C., Analytical solution to calculate the stress distribution in pin-and-collar samples bonded with anaerobic adhesives (following ISO 10123 standard), *International Journal of Adhesion and Adhesives*, 28, 2008, 405–410.
[19] Selahi, E., Elasticity solution of adhesive tubular joints in laminated composites with axial symmetry, *Archive of Mechanical Engineering*, 15, 2018, 441–456.
[20] Kurennov, S.S., Dvoretska, D.V., Axisymmetric Stress State of an Adhesive Joint of Two Coaxial Pipes. An Improved Theory, *Mechanics of Composite Materials*, 59, 2023, 495–506.
[21] Kumar, S., Khan, M., An elastic solution for adhesive stresses in multi-material cylindrical joints, *International Journal of Adhesion and Adhesives*, 64, 2016, 142–152.
[22] Shishesaz, M., Ghamarian, A.H., Mosalmani, R., The Effects of Defects and Adherend Material on Adhesive Stress Distribution in Laminated Composite Tubular Joints Under Axial Tensile Loads, *Journal of Applied and Computational Mechanics*, 11, 2025, 1112–1138.
[23] Pugno, N., Carpinteri, A., Tubular adhesive joints under axial load, *Transactions of the ASME – Journal of Applied Mechanics*, 70, 2003, 832–839.
[24] Nayeb-Hashemi, H., Rossettos, J.N., Melo, A.P., Multiaxial fatigue life evaluation of tubular adhesively bonded joints, *International Journal of Adhesion and Adhesives*, 17, 1997, 55–63.
[25] Spaggiari, A., Dragoni, E., Regularization of torsional stresses in tubular lap bonded joints by means of functionally graded adhesives, *International Journal of Adhesion and Adhesives*, 53, 2014, 23–28.
[26] Rao, M.D., Zhou, H., Vibration and damping of a bonded tubular lap joint, *Journal of Sound and Vibration*, 178, 1994, 577–590.
[27] Vaziri, A., Nayeb-Hashemi, H., Dynamic response of tubular joints with an annular void subjected to a harmonic torsional load, *Proceedings of the Institution of Mechanical Engineers, Part K: Journal of Multi-body Dynamics*, 216, 2002, 361–370.
[28] Vaziri, A., Nayeb-Hashemi, H., Dynamic response of tubular joints with an annular void subjected to a harmonic axial load, *International Journal of Adhesion and Adhesives*, 22, 2002, 367–373.
[29] Gunes, R., Apalak, M.K., Yildirim, M., Free vibration analysis of an adhesively bonded functionally graded tubular single lap joint, *Journal of Adhesion*, 87, 2011, 902–925.
[30] Tsai, M.Y., Oplinger, D.W., Morton, J., Improved theoretical solutions for adhesive lap joints, *International Journal of Solids and Structures*, 35, 1998, 1163–1185.
[31] Challita, G., Othman, R., Analytical model of the double-lap bonded joints response to harmonic loads, *European Journal of Mechanics - A/Solids*, 34, 2012, 149–158.
[32] Gafar, M.O., Almitani, K.H., Othman, R., Analytical model for harmonic response of dissimilar single-lap joints, *Proceedings of the Institution of Mechanical Engineers, Part K: Journal of Multi-body Dynamics*, 232, 2018, 457–472.

[33] Challita, G., Analytical study of the dynamic behavior of a voided adhesively bonded lap joint under axial harmonic load, *International Journal of Solids and Structures*, 141–142, 2018, 183–194.
[34] Almitani, K.H., Othman, R., Analytical solution of the harmonic response of visco-elastic adhesively bonded single-lap and double-lap joints, *International Journal of Adhesion and Adhesives*, 71, 2017, 55–65.
[35] Hazimeh, R., Khalil, K., Challita, G., Othman, R., Analytical model of double-lap bonded joints subjected to impact loads, *International Journal of Adhesion and Adhesives*, 57, 2015, 1–8.
[36] Wang, S., Guo, Q., Xie, Z., Extended analytical model for interfacial stresses of double-lap joints under harmonic loads, *International Journal of Adhesion and Adhesives*, 91, 2019, 23–35.
[37] Sindi, S.A., Othman, R., Almitani, K.H., Theoretical solution for the axial vibration of functionally graded double-lap adhesive joints, *Mathematics and Mechanics of Solids*, 26, 2021, 832–842.

ORCID iD

Ramzi Othman https://orcid.org/0000-0001-9037-5671

© 2026 Shahid Chamran University of Ahvaz, Ahvaz, Iran. This article is an open access article distributed under the terms and conditions of the Creative Commons Attribution-NonCommercial 4.0 International (CC BY-NC 4.0 license) (http://creativecommons.org/licenses/by-nc/4.0/).

How to cite this article: Othman R., et al., A Linear-shear-stress-based theoretical model for prediction of adhesive shear stress and dynamic axial response in tubular adhesive joints, *J. Appl. Comput. Mech.*, xx(x), 2026, 1–17. https://doi.org/10.22055/jacm.2026.48717.5450

Publisher's Note Shahid Chamran University of Ahvaz remains neutral with regard to jurisdictional claims in published maps and institutional affiliations.